Robotica (2022), **40**, pp. 1020–1035
doi:10.1017/S0263574721000989

CAMBRIDGE UNIVERSITY PRESS

ARTICLE

Kinematic modeling and solution of rigid-flexible and variable-diameter underwater continuous manipulator with load

Chen Yang, He Xu*, Xin Li and Fengshu Yu

College of Mechanical and Electrical Engineering, Harbin Engineering University, Harbin, China
*Corresponding author. E-mail: railway railway_dragon@sohu.com

Received: 29 December 2020; **Revised:** 4 May 2021; **Accepted:** 26 June 2021; **First published online:** 2 August 2021

Keywords: robot kinematics; soft actuator; hydraulic drive; optimization algorithm; deep learning.

Abstract

This paper presents a method to solve the kinematics of a rigid-flexible and variable-diameter continuous manipulator. The multi-segment underwater manipulator is driven by McKibben water hydraulic artificial muscle (WHAM). Considering the effect of elasticity and friction, we optimized the static mathematical model of WHAM. The kinematic model of the manipulator with load is established based on the hypothesis of piecewise constant curvature (PCC). We developed an optimization algorithm to calculate the length of the WHAMs according to the principle of minimum strain energy and obtain the configuration space parameters of the kinematic model. Based on the infinitesimal method, the homogeneous transformation matrices of the variable-diameter bending sections are computed, and the terminal position and attitude are obtained. In this paper, we studied the working space of the manipulator by quantitative analysis of the impact factors including pressure and load. A deep neural network (DNN) with six hidden layers is designed to solve inverse kinematics. The forward kinematic results are used to train and test the DNN, and the correlation coefficient between the output and target samples reaches 0.945. We carried out an underwater experiment and verified the effectiveness of the kinematic modeling and solution method.

Nomenclature

α, n	Braiding angle and the number of winding loops of the braided net
C_{10}	Parameter of the Neo-Hookean model
D	Diameter of the WHAM after pressurized
l,R	Length and inner radius of the rubber hose after pressurized
l_w	Length of the non-deformable section at both ends of the vertical WHAMs
p, p_e	Input pressure and external water pressure of the WHAM
$p_{ij}, N_{ij}, T_{ij}, U_{ij}, l_{ij}$	Input pressure, output force, horizontal force, elastic strain energy, and bending section length of the WHAMj in Segment$i$
$r_i^s, \theta_i^s, \phi_i^s$	Curvature radius, bending angle, and angle between the bending angle plane and the positive x-axis of infinitesimal$s$ in Segment i
T,b	Tension force and length of a single fiber of the braided net
σ_x, σ_z, F_g	Circumferential stress, axial stress, and axial contractile force of the rubber hose
A, E, t, V, R_0, l_0	Cross-sectional area, elastic modulus, wall thickness, volume, initial inner radius, and initial length of the rubber hose
F_N	Load force at the terminal plate of the manipulator
G_i	Gravity of the connecting plate O_i under water
k_f	Empirical friction coefficient

© The Author(s), 2021. Published by Cambridge University Press.

https://doi.org/10.1017/S0263574721000989 Published online by Cambridge University Press

l_{ij}^{s}	Length of WHAMj of infinitesimal$s$ in Segment i
N_0, N	Output force of the WHAM before and after improvement
θ_i, θ_{ii}	Bending angle between $O_i - 1$ plate and O_i plate and between O_0 plate and O_i plate
${}_{a}^{i}T, {}_{b}^{i}T, {}_{c}^{i}T$	Coordinate transformation matrix of the upper non-deformable section, the bending section, and the lower non-deformable section in Segment i

1. Introduction

Soft robotics is an emerging research field that develops rapidly in recent years [1] and has a wide application prospect because of its high flexibility and environmental adaptability. Its excellent characteristics make it have great potential in ocean exploration, medical care, service sector, and other fields [2–4].

Kinematic modeling of soft robots is challenging because of their characteristics of continuous nonlinear deformation and redundant degrees of freedom. The PCC model is still one of the most widely used soft robot models [5], based on which many applications have been added [6–8]. But the PCC model cannot describe the contractions motion of soft robots and is limited to describe the kinematics problem of constant curvature. Compared with the PCC model, the finite element model can more factually describe the nonlinear behavior of soft materials and visualize the deformation and force of the soft robots [9–11]. However, due to the high computational cost, its application is also limited. In addition to the commonly used methods, researchers proposed some innovative and effective modeling methods. A. Shiva et al. presented a comprehensive approach for modeling silicone-based soft continuum robotic appendages [12]. The paper also experimentally compared the effectiveness of elasticity versus hyperelasticity assumptions (Neo-Hookean and Gent) and concluded that Hooke's model best fits limited strains. A. Stilli et al. applied a beam mechanics-based model to soft stiffness controllable robots and takes into account various stiffness levels and interaction forces [13]. Gonthina et al. proposed a new approach to modeling variable curvature continuum robot sections based on Euler spirals and evaluated the approach by using the sections of numerous continuum robots [14]. The Euler spiral model is compared with the constant curvature model and the former was seen to be a significantly better match for a wide range of the robot hardware configurations. In the field of kinematic solution, the application of the artificial neural network (ANN) is increasing in recent years. With good performance in dealing with nonlinear tasks, ANN can obtain accurate kinematic solutions and identify the working space of the manipulator [15–17]. Besides, ANN also has a good application in the field of robot control technology [18,19].

In this paper, the forward and inverse kinematics of a rigid-flexible and variable-diameter manipulator with load is studied. The manipulator is designed for underwater working and uses WHAMs as soft actuators. The combination of rigidity and flexibility gives it a high-load capacity, and the variable-diameter characteristic allows it to swallow and disgorge objects [20]. We establish the kinematics model of the manipulator based on the well-known PCC model. To solve the forward kinematics, we design an optimization algorithm based on the principle of minimum strain energy and obtain the configuration space parameters. We obtain the homogeneous transformation matrices of the variable-diameter bending sections by the infinitesimal method and consider non-deformable sections into transformation matrices. Then the terminal position and attitude are computed by matrix multiplication. We figure out the working space under different impact factors and carry out comparative analyses. To solve the inverse kinematics, we design a DNN to solve the input pressure according to the target terminal position and attitude. And underwater experiment verification is carried out to verify the kinematic modeling and solution method.

2. Kinematic Modeling

2.1. Static theoretical model of WHAM

The force characteristics of the artificial muscles are related to the wall thickness, the geometrical features of end plugs, the friction, and other factors. In the previous modeling approach based on energy

https://doi.org/10.1017/S0263574721000989 Published online by Cambridge University Press

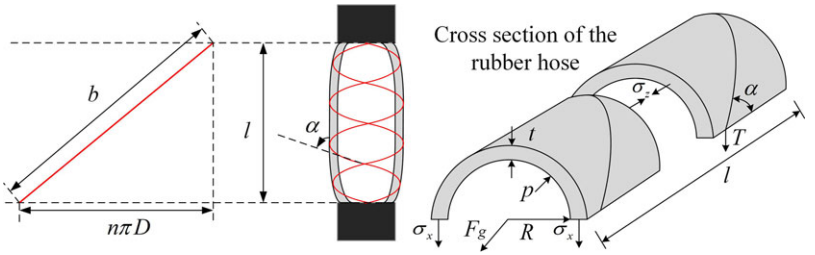


Figure 1. *Force analysis of WHAM considering elasticity.*

conservation, the effects of wall thickness and friction were ignored and the rubber hose was assumed to be an ideal cylinder. Considering the effect of water depth on artificial muscles, the output force of the artificial muscles in the previous theoretical model N_0 can be expressed as [21]

$$N_0 = \frac{\pi D^2 (p - p_e)(3\cos^2\alpha - 1)}{4} \tag{1}$$

To take the factor of elastic force produced by the rubber hose into account, the following assumptions are made [22,23]:

Assumption 2.1. *The strain and stress on the horizontal and vertical axes of the rubber hose are independent and satisfies the generalized Hooke's law;*

Assumption 2.2. *The thickness and volume of the rubber hose are constant and the gravity after pressurized is balanced with the buoyancy it receives underwater;*

Assumption 2.3. *The hydrodynamic effects can be ignored.*

Based on of the above assumptions, the force analysis of WHAM considering elastic force is shown in Fig. 1, and the force equilibrium equations are deduced as

$$\begin{cases} F_g + \pi R^2 (p - p_e) = \sigma_z A + T\cos\alpha \\ (p - p_e) lR = \sigma_z tl + nT\sin\alpha \end{cases} \tag{2}$$

Considering the impact of friction between the rubber hose and the braided net and between the fibers, the empirical friction coefficient K_f are introduced into the model [24]. The output force of the improved theoretical model N taking into account elasticity and friction can be expressed as:

$$N = (1 - k_f)\left(\frac{(p - p_e)(3l^2 - b^2)}{4\pi n^2} + \frac{VE}{l}\left(\frac{l}{l_0} - 1\right) + \frac{l^2 Et}{n\sqrt{b^2 - l^2}} - \frac{l^2 Et}{2\pi n^2 R_0}\right) \tag{3}$$

Under the same input pressure, the comparison of the relationship between output force and contraction rate ($\frac{l_0 - l}{l_0}$) of WHAM in the previous model and the improved model is shown in Fig. 2. When the contraction rate is 0, the output force is smaller in the improved model. And when the output force is zero, the contraction rate in the previous model is 0.330, and that in the improved model is 0.268.

2.2. Kinematic model of the continuous manipulator

Figure 3 shows the structural model of the continuous manipulator studied in this paper. Each rigid-flexible segment consists of a bending section and two non-deformable sections, including three vertical WHAMs and three horizontal ones. The paper refer to the two non-deformable sections connecting the bending sections of the upper and the lower two segments as a connecting plate. In each connecting plate, three horizontal WHAMs and 3D-printed components make up a variable-diameter gripper. When the transverse muscles are pressurized, the diameter of the gripper decreases to grasp objects. The manipulator can bend in different positions and attitudes by inputting different combinations of pressure to

https://doi.org/10.1017/S0263574721000989 Published online by Cambridge University Press

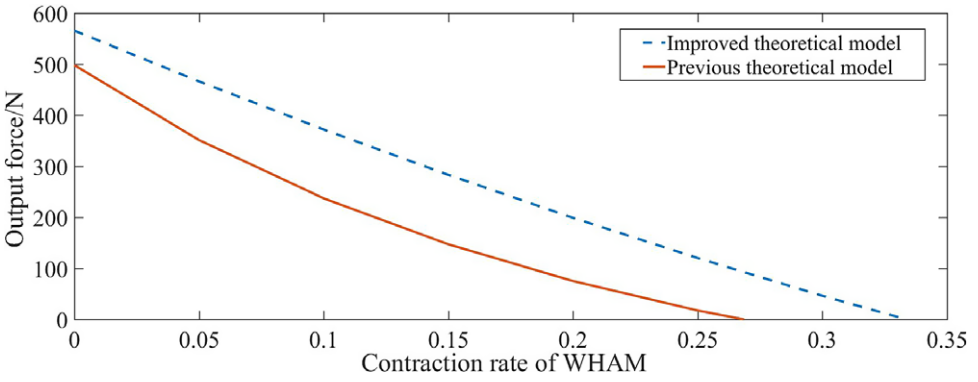


Figure 2. *Comparison of the relationship between output force and contraction rate of WHAM in the previous model and the improved model under the same input pressure.*

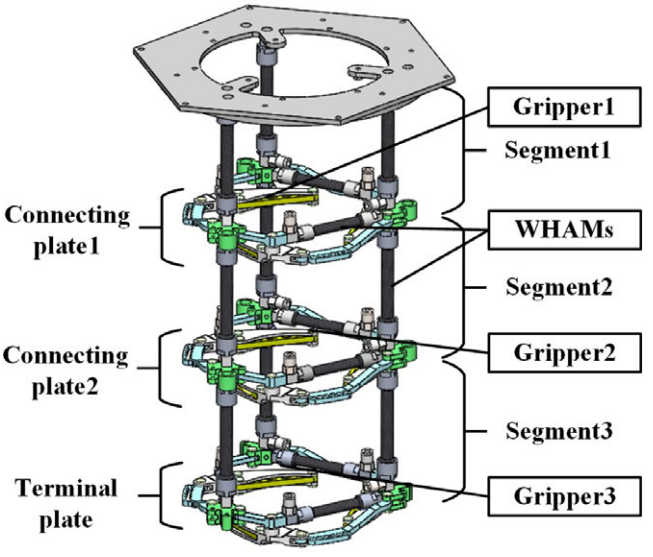


Figure 3. *Structural model of the manipulator.*

the vertical muscles. Table I shows the changes in the position and attitude of the manipulator under different input pressures of WHAMs. And by the cooperation of the vertical and horizontal muscles, the manipulator can swallow and disgorge objects in imitation of the action of snakes. The characteristics of the rigid-flexible structural make the manipulator keep flexible and have specific stiffness to improve its load capacity. See more details about the manipulator in this paper [20].

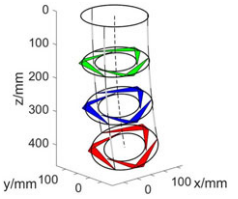
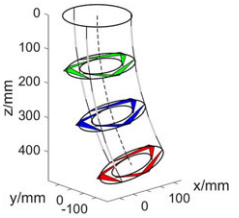
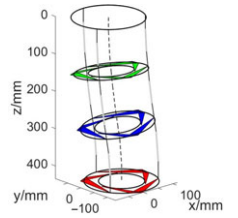
The PCC model can be applied to manipulators with non-deformable sections between the bending sections [25]. In the PCC model, the bending section composed of WHAMs can be considered as joined segments of constant curvature (CC). The following two assumptions are made to predict the bending deformation and spatial position based on the PCC model [26]:

Assumption 2.4. *The centerline of the bending section and the WHAMs are equal curvature arc in each segment;*

Assumption 2.5. *The central axes and bending plane of the three WHAMs of each segment are parallel to each other.*

https://doi.org/10.1017/S0263574721000989 Published online by Cambridge University Press

Table I. *Manipulator input pressure and the corresponding position and attitude.*

Input pressure of vertical WHAMs	Terminal position and attitude
*Segment*1:0*MPa*, 0*MPa*, 1*MPa*; *Segment*2:0*MPa*, 0*MPa*, 1*MPa*; *Segment*3:0*MPa*, 0*MPa*, 1*MPa*;	
*Segment*1:1*MPa*, 0*MPa*, 1*MPa*; *Segment*2:1*MPa*, 0*MPa*, 1*MPa*; *Segment*3:1*MPa*, 0*MPa*, 1*MPa*;	
*Segment*1:0*MPa*, 1*MPa*, 1*MPa*; *Segment*2:1*MPa*, 0*MPa*, 1*MPa*; *Segment*3:1*MPa*, 1*MPa*, 0*MPa*;	

For the continuous manipulator in this paper with n segments, the kinematic model is established as shown in Fig. 4(a). According to the PCC model, the paper set up reference coordinate systems in various segments to describe the changes of the position and attitude through the homogeneous transformation matrices. All reference coordinate systems are established by the same standard, their x-axis all passes through a WHAM on the same side. The homogeneous transformation matrices are represented by three configuration space parameters, which are curvature radius r_i, bending angle θ_i, and the angle between the bending plane and the positive X_i-axis ϕ_i (i =1,2. . .,n). The three WHAMs in each segment are defined as WHAM1, WHAM2, and WHAM3. Then for the WHAMj (j=1,2,3) of Segment$i$, its length, input pressure, output force, and constraint reaction force are defined as l_{ij}, p_{ij}, N_{ij}, and T_{ij} respectively. Take all the structure between O_i disk and O_n disk as a whole part, Fig. 4(b) shows its force analysis when underwater working with load force. The whole part is affected by the load force F_N, the gravity of each connecting plate G_i under water (considering buoyancy), the output forces of the WHAMs N_{ij}, and the constraint reaction forces of the WHAMs T_{ij}. The force balance equations can be listed as follows:

$$\begin{cases} (F_N + \sum_{k=i}^{n} G_k)\cos(\theta_{ii}) = \sum_{j=1}^{3} N_{ij} \\ (F_N + \sum_{k=i}^{n} G_k)\sin(\theta_{ii}) = \sum_{j=1}^{3} T_{ij} \end{cases} \tag{4}$$

The ends of the WHAMs are installed perpendicular to the connecting plates, so the output force N_{ij} acts perpendicular to connecting plate O_i and the constraint reaction force T_{ij} acts parallel to connecting plate O_i. The component forces of the gravity and load force perpendicular to the connecting plates are balanced with the output forces. Since N_{ij} is determined by the input pressure and the length of the WHAM, the first force balance equation determines the length of the WHAMs when the input pressure is given. The component forces of gravity and load force parallel to the connecting plates are balanced

https://doi.org/10.1017/S0263574721000989 Published online by Cambridge University Press

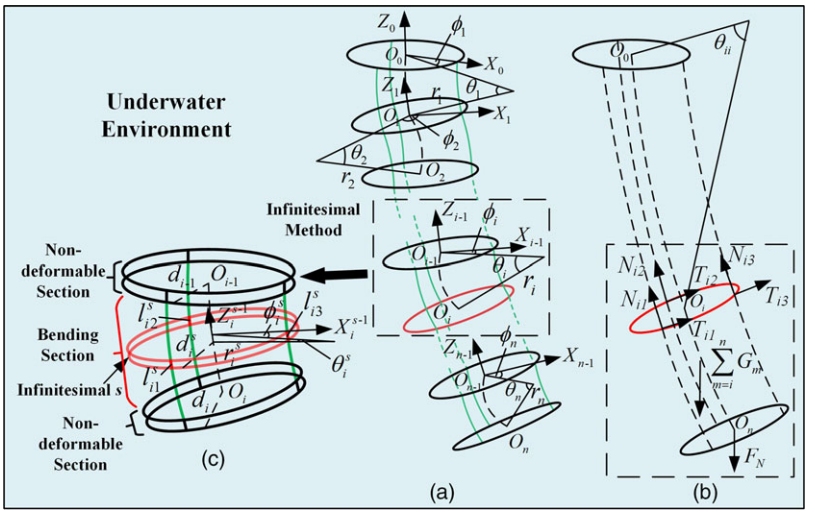


Figure 4. *Kinematic model and force analysis of the underwater manipulator with load.*

with the constrained reaction forces. Because the forces are perpendicular to the ends of the WHAMs, the second force balance equation does not affect the length of the WHAMs within a specific range. The bending angles θ_i, θ_{ii} are also the minimum dihedral angles between the connecting plates. The value of the minimum dihedral angles can be expressed by the geometric relationship with the length of the WHAMs. While θ_{ii} is the minimum dihedral angle between the O_i plate and the O_0 plate on the horizontal plane, when $0 \le \theta_{ii} \le 0.5\pi$, the range of θ_{ii} can be expressed as

$$\theta_{ii} \ge \theta_1 + \theta_2 + ... + \theta_i \tag{5}$$

Substitute Eq. (5) into Eq. (4). When the input pressure is given, the solution interval of the length of the WHAMs can be expressed as

$$\begin{cases} N_{11} + N_{12} + N_{13} = (F_N + \sum_{k=1}^{n} G_k)\cos(\theta_1) \\ N_{i1} + N_{i2} + N_{i3} \le (F_N + \sum_{p=i}^{n} G_p)\cos(\sum_{q=1}^{n} \theta_q) \end{cases} \quad (i = 2, 3, ..., n) \tag{6}$$

where $\theta_i = f(l_{ij})$

$N_{ij} = g(l_{ij}, p_{ij}) \quad (i = 1, 2, ..., n; j = 1, 2, 3)$

3. Kinematic Solution

3.1. Forward kinematic solution

For linear elastic statically indeterminate systems with unknown loading processes, the principle of minimum strain energy is valid as long as the system is in a stable state under the final load. The system has the condition that the strain energy of the whole system is minimized. Therefore, the minimum elastic strain energy of WHAMs in the process of pressurization and loading is set as the optimization function to obtain the solution of the length of the WHAMs. According to the strain energy function of silicon rubber material described by the neo-Hookean model, the strain energy function of WHAMs can be expressed as [27]

$$U_{ij} = C_{10}\left(\frac{l_{ij}^2}{l_0^2} + \frac{b^2 - l_{ij}^2}{4\pi^2 n^2 R_0^2} - 2\right) \quad (i = 1, 2, ..., n; j = 1, 2, 3) \tag{7}$$

https://doi.org/10.1017/S0263574721000989 Published online by Cambridge University Press

The original length of WHAMs before pressurized is specified as the rated maximum working length. The optimization algorithm can be expressed as

$$\begin{aligned}
&\mathbf{X} = \left[l_{11}, l_{12}, l_{13}, l_{21}, ..., l_{ij}\right]^T \quad (i = 1, 2, ..., n; j = 1, 2, 3)\\
&\min f(\mathbf{X}) = \sqrt[2]{\frac{\sum_{i=1}^{n}\sum_{j=1}^{3} U_{ij}}{n}}\\
&\text{s.t. } h(\mathbf{X}) = (F_N + \sum_{k=1}^{n} G_k)\cos(\theta_1) - \sum_{j=1}^{3} N_{1j} = 0\\
&\quad g^1(\mathbf{X}) = \sum_{j=1}^{3} N_{ij} - (F_N + \sum_{p=i}^{n} G_p)\cos(\sum_{q=1}^{i}\theta_q) \le 0\\
&\quad g^2(\mathbf{X}) = N_{ij} \ge 0
\end{aligned} \tag{8}$$

To solve the configuration space parameters, the bending section of each segment is divided into m infinitesimals as shown in Fig. 4(c). The length of three WHAMs in infinitesimal$s$ is $l_{ij}^s = \frac{l_{ij}}{m}$. The cross-sectional radius of each infinitesimal d_i^s varies gradually with s and can be expressed by the length of the transverse muscles. According to the geometric relationship, the configuration space parameters in each infinitesimal $r_i^s, \theta_i^s, \phi_i^s$ can be expressed as

$$\begin{cases}
r_i^s = \dfrac{(l_{i1}^s + l_{i2}^s + l_{i3}^s)d_i^s}{2\sqrt{\sum_{j=1}^{3}\left(l_{ij}^s\right)^2 - l_{i1}^s l_{i2}^s - l_{i2}^s l_{i3}^s - l_{i1}^s l_{i3}^s}}\\
\theta_i^s = \dfrac{2\sqrt{\sum_{j=1}^{3}\left(l_{ij}^s\right)^2 - \left(l_{i1}^s\right)^2\left(l_{i2}^s\right)^2 - \left(l_{i2}^s\right)^2\left(l_{i3}^s\right)^2 - \left(l_{i1}^s\right)^2\left(l_{i3}^s\right)^2}}{3d_i^s} \quad (i = 1, 2, ..., n; j = 1, 2, 3; s = 1, 2, ..., m)\\
\phi_i^s = \begin{cases}
\arctan\dfrac{\sqrt{3}(l_{i2}^s + l_{i3}^s - 2l_{i1}^s)}{3(l_{i2}^s - l_{i3}^s)} (l_{i2}^s \ne l_{i3}^s)\\
-0.5\pi\,(l_{i2}^s = l_{i3}^s < l_{i1}^s)\\
0.5\pi\,(l_{i2}^s = l_{i3}^s > l_{i1}^s)
\end{cases}
\end{cases} \tag{9}$$

The coordinate transformation matrix of each infinitesimal ${}_i^sT$ can be expressed by the configuration space parameters as

$$\begin{aligned}
{}_i^sT &= \mathrm{Rot}(z, \phi_i^s)\mathrm{Rot}(y, \theta_i^s)\mathrm{Trans}(r_i^s(1 - \mathrm{c}\theta_i^s), 0, r_i^s\mathrm{s}\theta_i^s)\mathrm{Rot}(z, -\phi_i^s)\\
&= \begin{bmatrix}
\cos^2\phi_i^s(\cos\theta_i^s - 1) + 1 & \sin\phi_i^s\cos\phi_i^s(\cos\theta_i^s - 1) & \cos\phi_i^s\sin\theta_i^s & r_i^s\cos\phi_i^s(1 - \cos\theta_i^s)\\
\sin\phi_i^s\cos\theta_i^s(\cos\theta_i^s - 1) & \cos^2\phi_i^s(1 - \cos\theta_i^s) + \cos\theta_i^s & \sin\phi_i^s\sin\theta_i^s & r_i^s\sin\phi_i^s(1 - \cos\theta_i^s)\\
-\cos\phi_i^s\sin\theta_i^s & -\sin\phi_i^s\sin\theta_i^s & \cos\theta_i^s & r_i^s\sin\theta_i^s\\
0 & 0 & 0 & 1
\end{bmatrix}\\
&\quad (i = 1, 2, ..., n; s = 1, 2, ..., m)
\end{aligned} \tag{10}$$

The coordinate transformation matrices of the non-deformable section at both ends of each segment ${}_a^iT, {}_c^iT$ are represented by transformation matrices. Then the terminal position and attitude matrix ${}^nT$ can be expressed as

$${}^nT = \prod_{i=1}^{n} {}_a^iT_b^iT_c^iT \tag{11}$$

https://doi.org/10.1017/S0263574721000989 Published online by Cambridge University Press

$$\begin{cases} {}^{i}_{b}T = \prod_{s=1}^{m} {}^{s}_{i}T \\ {}^{i}_{a}T = {}^{i}_{c}T = \begin{bmatrix} 1 & 0 & 0 & 0 \\ 0 & 1 & 0 & 0 \\ 0 & 0 & 1 & l_w \\ 0 & 0 & 0 & 1 \end{bmatrix} \end{cases} (i = 1, 2, ..., n) \tag{12}$$

For the terminal position and attitude matrix

$${}^{n}T = \begin{bmatrix} e_1 & e_4 & e_7 & e_{10} \\ e_2 & e_5 & e_8 & e_{11} \\ e_3 & e_6 & e_9 & e_{12} \\ 0 & 0 & 0 & 1 \end{bmatrix}$$

where $e_k = g(l_{ij})$ $(k = 1, 2, ..., 12)$

$l_{ij} = f(p_{ij}, N_{ij})$ $(i = 1, 2, ..., n; j = 1, 2, 3)$

Its terminal position and attitude ${}^{n}\gamma$ can be expressed as

$${}^{n}\gamma = \begin{bmatrix} x \\ y \\ z \\ \delta \\ \beta \\ \psi \end{bmatrix} = \begin{bmatrix} e_{10} \\ e_{11} \\ e_{12} \\ \text{atan2}(e_6, e_9) \\ \text{atan2}(-e_3, \sqrt{e_1^2 + e_2^2}) \\ \text{atan2}(e_2, e_1) \end{bmatrix} \tag{13}$$

δ, β, ψ are roll angle, pitch angle, and yaw angle, respectively. For the continuum manipulator with three segments studied in this paper, the solution process is shown in Fig. 5. p_{h1}, p_{h2}, p_{h3} is the input pressures of the horizontal WHAMs in Segment1, Segment2, Segment3.

Theoretically, the larger the value of the infinitesimal number m, the more accurate the model will be, but the computational time will be significantly longer. With the increase of m, the computed result changed significantly and then tended to be stable. When m is greater than 30, the change of computed result becomes very small. Considering both the computational time and the accuracy of the model, m is set as 100.

3.2. Forward kinematics case study

This section presents five groups of calculation results as a case study for comparison, as shown in Table II. The first three groups correspond to the results caused by proportional changes of input pressure under the same load force. The last three groups correspond to the results of different load forces under the same input pressure.

3.3. Inverse kinematic solution

The inverse kinematic solution process is to solve input pressures of the manipulator according to the given terminal position and attitude and load force. Also, the input pressure of the variable-diameter grippers should be given as a known condition. The solution process of inverse kinematics can be expressed as

https://doi.org/10.1017/S0263574721000989 Published online by Cambridge University Press

Table II. *Input pressure and corresponding terminal position and attitude.*

Input pressure matrix/MPa	Load force/N	Artificial muscle length matrix/mm	Terminal position and attitude matrix/mm
$\begin{bmatrix} 0.6 & 0.3 & 0.6 \\ 0.6 & 0.3 & 0.6 \\ 0.6 & 0.3 & 0.6 \end{bmatrix}$	115	$\begin{bmatrix} 65.0911 & 72.8060 & 69.0793 \\ 69.4081 & 72.4688 & 64.8935 \\ 65.2093 & 72.4619 & 68.8514 \end{bmatrix}$	$\begin{bmatrix} 0.9958 & -0.0033 & 0.0913 & 20.7645 \\ -0.0035 & 0.9972 & 0.0745 & 17.2638 \\ -0.0913 & -0.0746 & 0.9930 & 442.6256 \\ 0 & 0 & 0 & 1 \end{bmatrix}$
$\begin{bmatrix} 0.8 & 0.4 & 0.8 \\ 0.8 & 0.4 & 0.8 \\ 0.8 & 0.4 & 0.8 \end{bmatrix}$	115	$\begin{bmatrix} 64.8610 & 69.1385 & 65.7496 \\ 64.0616 & 69.3067 & 66.2379 \\ 63.9803 & 70.7800 & 64.8263 \end{bmatrix}$	$\begin{bmatrix} 0.9971 & -0.0025 & 0.0760 & 14.6665 \\ -0.0029 & 0.9974 & 0.0715 & 14.6736 \\ -0.0760 & -0.0716 & 0.9945 & 435.9267 \\ 0 & 0 & 0 & 1 \end{bmatrix}$
$\begin{bmatrix} 1.0 & 0.5 & 1.0 \\ 1.0 & 0.5 & 1.0 \\ 1.0 & 0.5 & 1.0 \end{bmatrix}$	115	$\begin{bmatrix} 63.8294 & 69.0246 & 64.3649 \\ 63.8488 & 69.2410 & 64.0161 \\ 64.1247 & 67.7890 & 64.7268 \end{bmatrix}$	$\begin{bmatrix} 0.9969 & -0.0022 & 0.0793 & 18.9304 \\ -0.0021 & 0.9985 & 0.0550 & 12.9011 \\ -0.0793 & -0.0550 & 0.9953 & 433.1769 \\ 0 & 0 & 0 & 1 \end{bmatrix}$
$\begin{bmatrix} 1.0 & 0.5 & 1.0 \\ 1.0 & 0.5 & 1.0 \\ 1.0 & 0.5 & 1.0 \end{bmatrix}$	500	$\begin{bmatrix} 70.3041 & 70.0583 & 68.8440 \\ 68.6394 & 71.0938 & 69.5095 \\ 69.9146 & 68.8266 & 69.9146 \end{bmatrix}$	$\begin{bmatrix} 0.9999 & -0.0001 & 0.0105 & 4.4471 \\ 0.0000 & 1.0000 & 0.0019 & 0.1225 \\ -0.0105 & -0.0019 & 0.9999 & 446.0019 \\ 0 & 0 & 0 & 1 \end{bmatrix}$
$\begin{bmatrix} 1.0 & 0.5 & 1.0 \\ 1.0 & 0.5 & 1.0 \\ 1.0 & 0.5 & 1.0 \end{bmatrix}$	1000	$\begin{bmatrix} 74.9525 & 72.5205 & 75.8083 \\ 75.1130 & 76.2208 & 74.9385 \\ 74.9699 & 76.1473 & 74.9697 \end{bmatrix}$	$\begin{bmatrix} 1.0000 & 0.0000 & -0.0049 & -5.3182 \\ -0.0000 & 1.0000 & 0.0019 & -1.0232 \\ 0.0049 & -0.0019 & 1.0000 & 462.1713 \\ 0 & 0 & 0 & 1 \end{bmatrix}$

$$ {}^{n}\gamma = \begin{bmatrix} x \\ y \\ z \\ \delta \\ \beta \\ \psi \end{bmatrix} ; F_N = [F_N] ; {}^{H}P = \begin{bmatrix} p_{h1} - p_e \\ p_{h2} - p_e \\ p_{h3} - p_e \end{bmatrix} \Rightarrow {}^{V}P = \begin{bmatrix} p_{11} - p_e & p_{12} - p_e & p_{13} - p_e \\ p_{21} - p_e & p_{22} - p_e & p_{23} - p_e \\ p_{31} - p_e & p_{32} - p_e & p_{33} - p_e \end{bmatrix} \tag{14} $$

Due to the complexity of calculation and many variables and matrix operations, it is very complex and difficult to solve inverse kinematics by inverse derivation. A DNN is designed to solve the inverse kinematics in this paper. In the DNN, the terminal position and attitude $x, y, z, \delta, \beta, \psi$ and the input pressures of the grippers ${}^{H}P$ are input, and the input pressures of the vertical muscles ${}^{V}P$ in the three segments are output. The TensorFlow library of Python is used to build the DNN. The DNN has 10 input nodes: the terminal position and attitude, load force, and input pressures of the grippers in the three segments $x, y, z, \delta, \beta, \psi, F_N, p_{h1}, p_{h2}, p_{h3}$. To unify the dimensions, training data are normalized before input. The output node has nine nodes: the input pressures of the vertical muscles in the three segments $p_{11}, p_{12}, p_{13}, p_{21}, p_{22}, p_{23}, p_{31}, p_{32}, p_{33}$. The DNN can be expressed as

$$ {}^{V}P = \mathrm{DNN_Net}({}^{3}\gamma, {}^{H}P) \tag{15} $$

https://doi.org/10.1017/S0263574721000989 Published online by Cambridge University Press

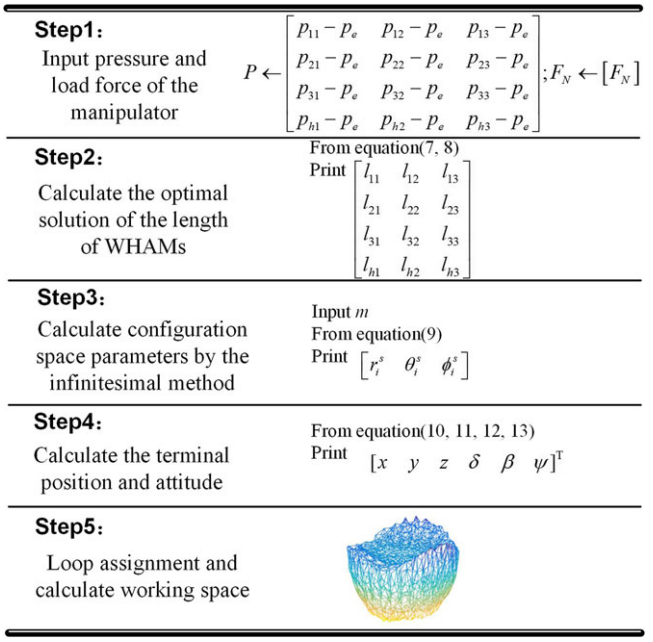


Figure 5. *Forward kinematic solution process.*

The network has 6 hidden layers, each with 200 nodes. ADAM optimization algorithm is selected as the training method. RELU activation function is selected as the activation function of the hidden layers and linear activation function is selected in the output layer. To avoid overfitting and ensure generalization ability, Batch Normalization (BN) layers are constructed and the net is trained in batches. Mean Square Error (MSE) is selected as the loss function. Ninety-thousand forward kinematic calculation results in the working space are randomly chosen as the training set. At training epoch 12,000, the MSE dropped to $7e^{-4}$. Another 10,000 forward kinematic results are input to the model as the testing set to test the network's performance, and the correlation coefficient between the output and target samples reaches 0.945.

4. Analysis of Impact Factors of Working Space

4.1. Characteristics of working space

According to the calculation process as shown in Fig. 5, the terminal position and attitude of the underwater manipulator with three segments studied in this paper are calculated. By loop assignment of input pressure and load force, the terminal coordinates are plotted, and the working space of the manipulator is figured out. As shown in Fig. 6, the working place of the manipulator is a bowl-shaped entity with a symmetrical center and an undulating edge. Point *A*, *B*, and *C* are convex points obtained with the maximum input pressure on one side and the minimum input pressure on the other two sides. Point *D*, *E*, and *F* are concave points obtained with the maximum input pressure on two sides and the minimum input pressure on the other side. Point *G* is the lowest point of the depression on the surface and is obtained when all input pressures are at the maximum value.

4.2. Effect of load force on working space

Figure 7 shows the effect of the load force F_N on the working space under the same maximum of input pressure $p_{\max}$. The load forces are selected according to the actual application of the manipulator. For

https://doi.org/10.1017/S0263574721000989 Published online by Cambridge University Press

Table III. *Effect of load force on working space.*

p_{max}/MPa	**Different loading forces/N**	**Proportion of working space volume**
0.4	0;115;500;784	1;0.972;0.892;0.600
0.6	0;115;500;1000;1145	1;0.960;0.828;0.543;0.516
0.8	0;115;500;1000;1396	1;0.960;0.830;0.634;0.585
1.0	0;115;500;1000;1598	1;0.958;0.826;0.777;0.663

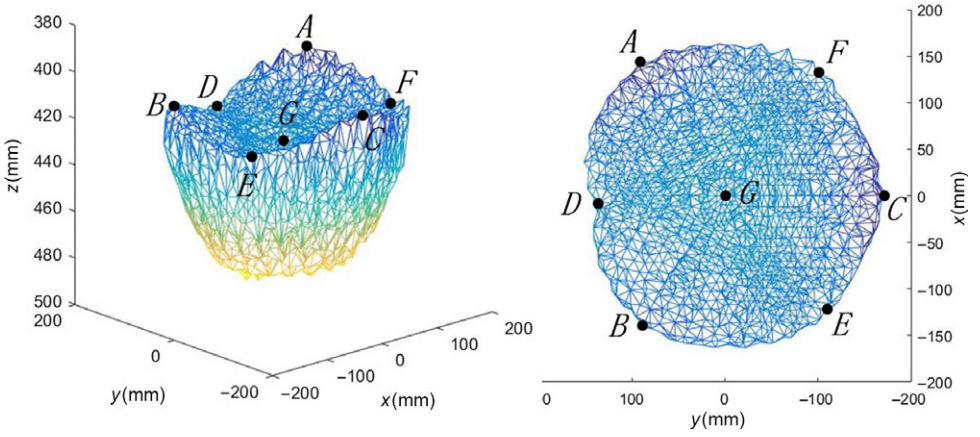


Figure 6. *Working space with special points.*

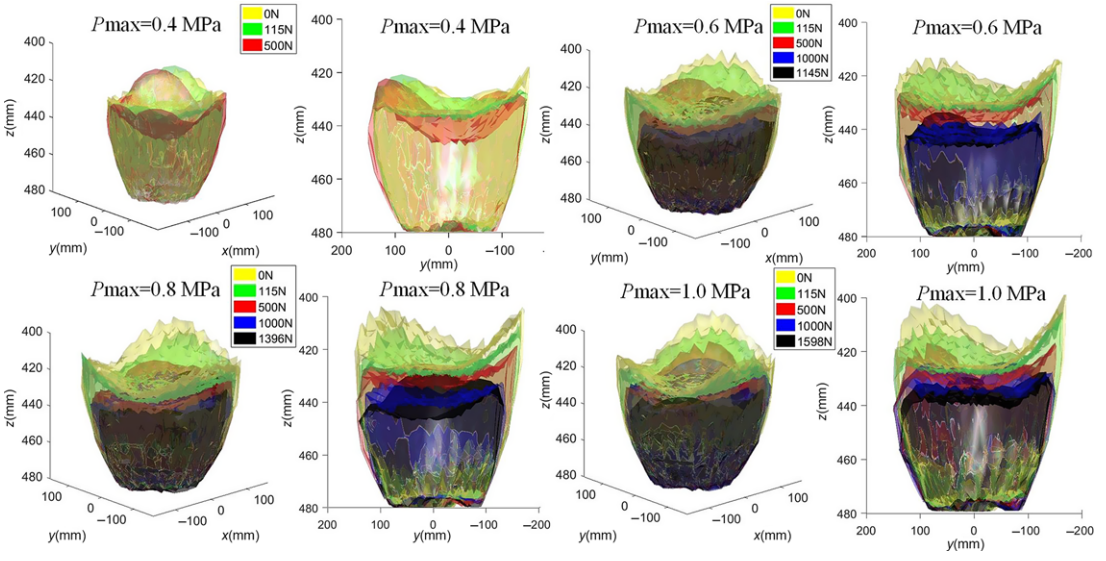


Figure 7. *Effect of the load force on working space.*

easy understanding, cross-section figures are added to the right side of the three-dimensional figures. With the increase of the load force, the working space of the manipulator becomes smaller. The paper compute the volume of the workspaces and compared the effects of impact factors in proportion, as shown in Table III.

https://doi.org/10.1017/S0263574721000989 Published online by Cambridge University Press

Table IV. *Effect of maximum input pressure on working space.*

F_N	Different input pressures/MPa	Proportion of working space volume
0	1.0;0.8;0.6;0.4;0.2	1;0.981;0.890;0.763;0.492
115	1.0;0.8;0.6;0.4;0.2	1;0.983;0.893;0.774;0.481
500	1.0;0.8;0.6;0.4	1;0.985;0.893;0.788
1000	1.0;0.8;0.6;0.4	1;0.801;0.623;0.590

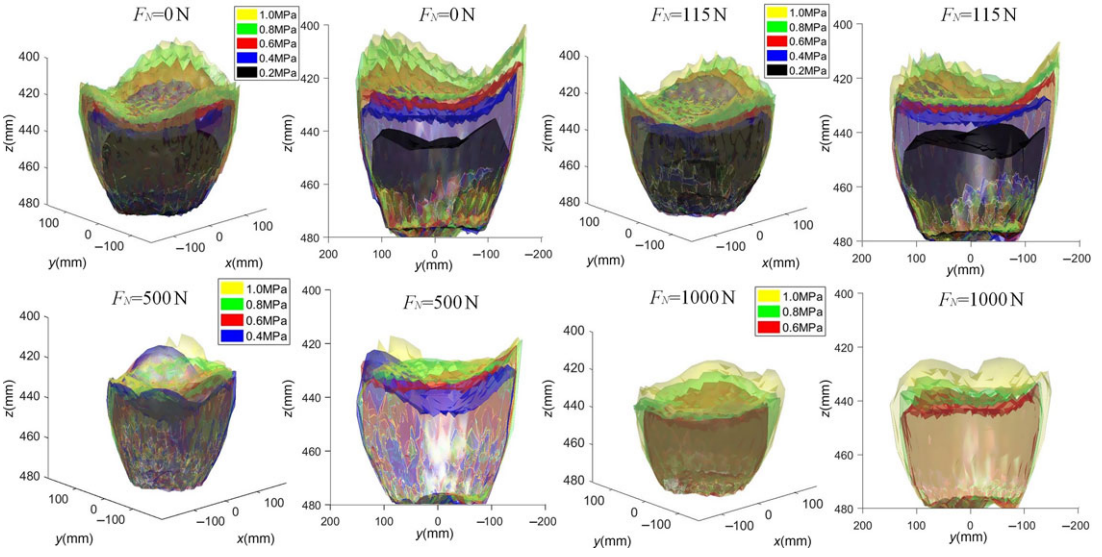


Figure 8. *Effect of the maximum input pressure on working space.*

4.3. Effect of maximum input pressure and water depth on working space

For the input pressure matrix of the underwater manipulator

$$ {}^{I}P = \begin{bmatrix} p_{11} - p_e & p_{12} - p_e & p_{13} - p_e \\ p_{21} - p_e & p_{22} - p_e & p_{23} - p_e \\ p_{31} - p_e & p_{32} - p_e & p_{33} - p_e \\ p_{h1} - p_e & p_{h2} - p_e & p_{h3} - p_e \end{bmatrix} $$

When $p_{\max}$ increases, the working space of the underwater manipulator also increases. At the same time, as the water depth increases, the external pressure p_e increases, which is equivalent to reducing the effective input pressure of the WHAMs. Each increase in a water depth of 10 m is approximately equal to a reduction in the maximum input pressure of 0.1 MPa. Figure 8 and Table IV show the effect of $p_{\max}$ on the working space under the same load force.

4.4. Maximum load force and the rate of no solution points

As shown in Fig. 9(a), with the increase of $p_{\max}$, the maximum load force $F_{N\max}$ that the manipulator can bear also increases. Under the maximum input pressure of 1.0 MPa, $F_{N\max}$ reaches 1598 N. With the change of the given load force and the maximum input pressure, the rate of no solution points in all input data sets also changes. As shown in Fig. 9(b), the greater the maximum input pressure, the less the no solution points under the same load force.

https://doi.org/10.1017/S0263574721000989 Published online by Cambridge University Press

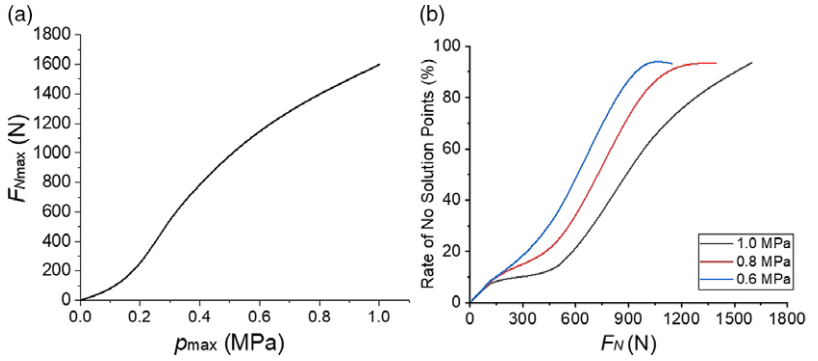


Figure 9. *(a) Relationship between maximum load force and input pressure; (b) Effects of load force and input pressure on no solution points.*

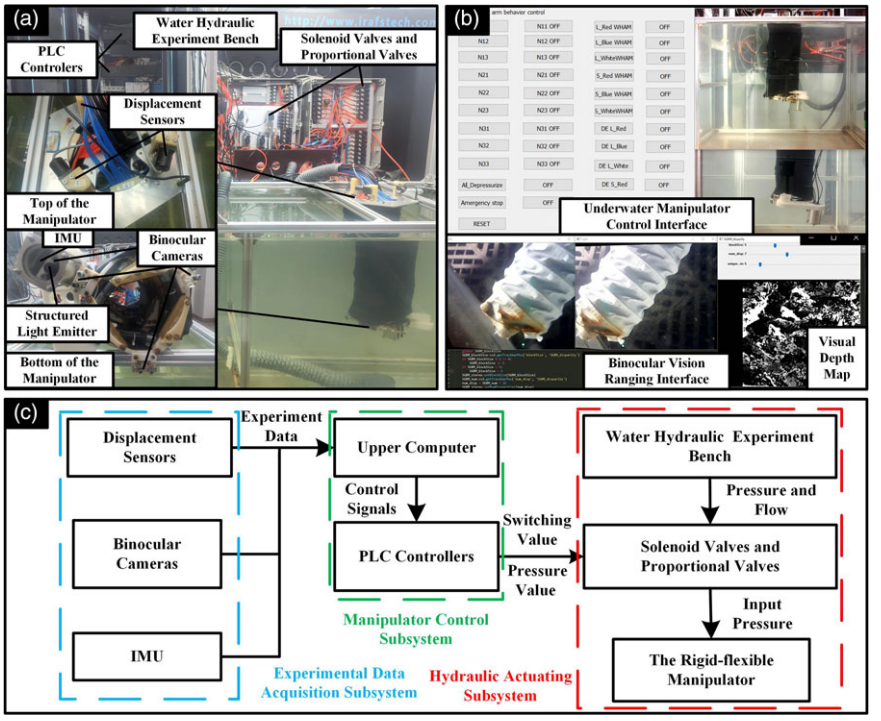


Figure 10. *(a) Experimental system setups; (b) Software interface; (c) Experimental subsystems.*

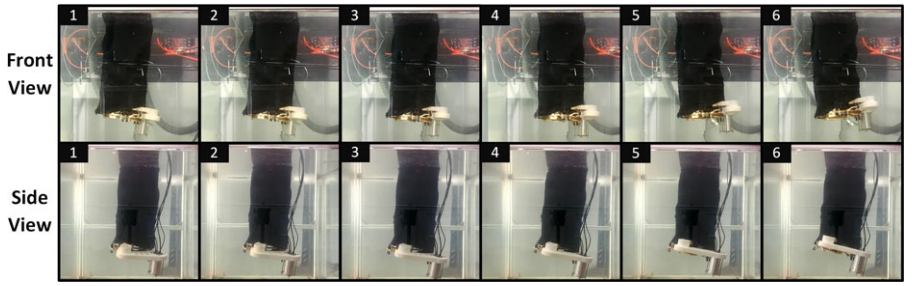


Figure 11. *Position and attitude of the manipulator under different maximum input pressures.*

https://doi.org/10.1017/S0263574721000989 Published online by Cambridge University Press

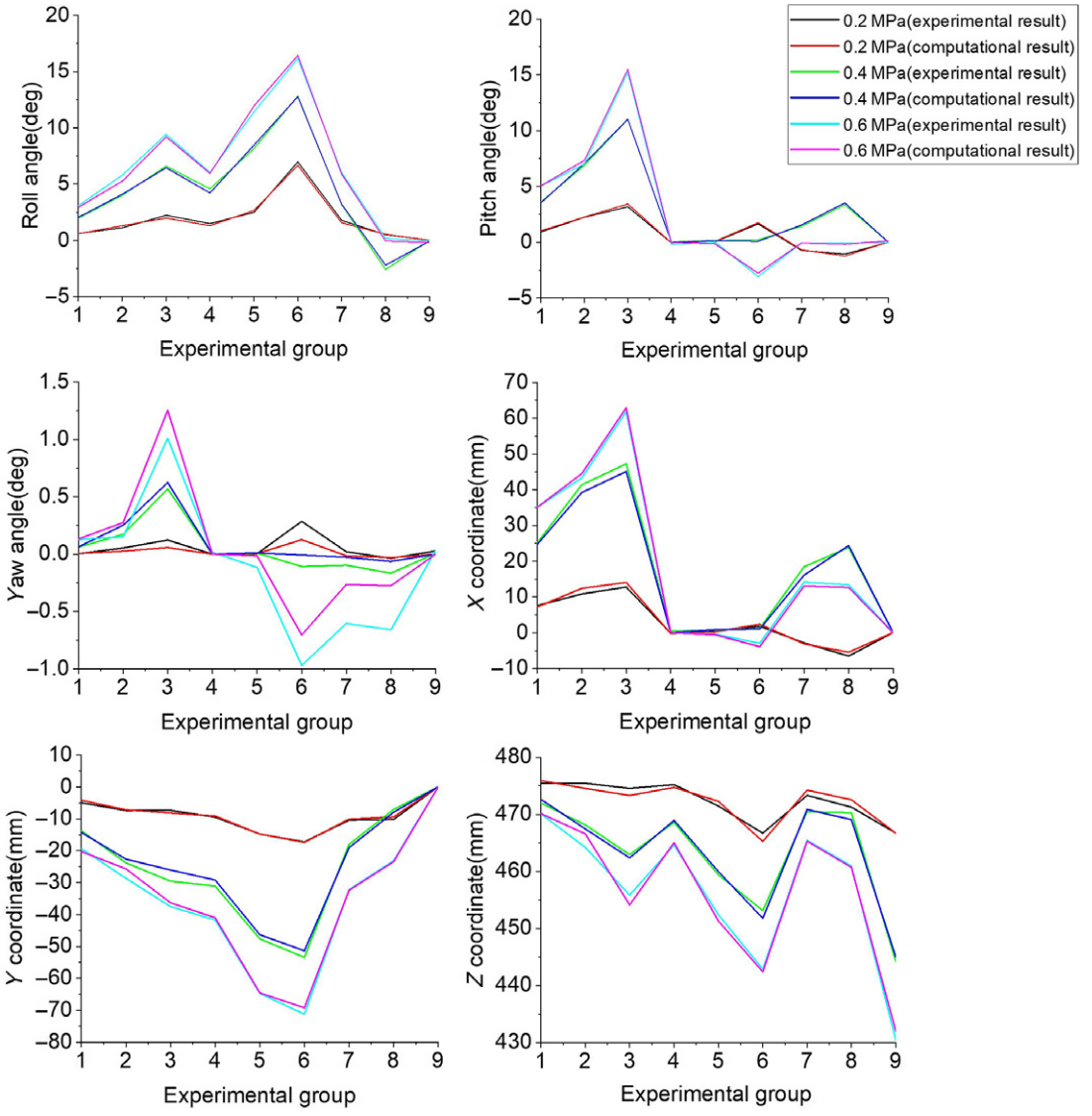


Figure 12. *Comparison of experimental results and computational results.*

5. Experimental Verification

Experimental setups are shown in Fig. 10(a). The top of the manipulator is equipped with three pull-rope displacement sensors connecting the top plate and the terminal plate. For observing the external situation and measuring the distance, three binocular cameras are installed in different directions at the bottom of the manipulator. A lightweight integrated sensor is placed on the terminal plane, which contains an inertial measurement unit (IMU), a structured light emitter, and a binocular camera. The IMU measures the terminal attitude angles and the acceleration changes during the movement of the manipulator, and the terminal position is obtained by location compute. The binocular cameras are used to observe the target object and the environment around the manipulator and can provide accurate distance measurement. The structured light emitter provides structured light to assist the binocular camera to measure distance. All equipment in the experiment has been waterproofed and can work underwater for long periods. As shown in Fig. 10(b), the underwater manipulator control software and the binocular vision ranging software are developed. The underwater manipulator control software is used to control the manipulator to

https://doi.org/10.1017/S0263574721000989 Published online by Cambridge University Press

achieve different positions and attitudes, and the binocular vision ranging software is used to observe the external environment and measure distance information in real time. The experimental subsystems and their relationship are shown in Fig. 10(c). The upper computer collects experimental data and controls PLC through serial ports and then controls the solenoid valves and proportional valves through PLC. The input pressure of the manipulator is provided by the water hydraulic experiment bench and the pressure and flow are controlled by the valves. Figure 11 shows the pose of the manipulator under different input pressure combinations.

The results of kinematics computation under different maximum input pressures are verified. The validation includes both boundary points and internal points in the working space of the manipulator. The comparison between the computational data and the experimental data under different maximum input pressures is shown in Fig. 12. The experiment groups in the horizontal coordinates correspond to the same boundary point or internal point under different pressures. The vertical coordinates correspond to the terminal attitude and position. As can be seen in the figure, the experimental results are in good agreement with the computational results. In all effective results, the maximum attitude error is no more than 1° and the maximum position error is no more than 5mm. The experiment proved the accuracy of the kinematics modeling and solution method.

6. Conclusion

This paper presents a method to solve forward and inverse kinematics of rigid-flexible continuous manipulator. The manipulator is hydraulically driven and can perform high-load underwater operations. The theoretical model of WHAM is improved by combining friction and elasticity, and the kinematics model of the manipulator is established based on the PCC model. Based on the principle of minimum strain energy, we design an optimization algorithm to solve the length of soft actuators and then derive the configuration space parameters of the model. We compute the homogeneous transformation matrices of the variable-diameter bending sections based on the infinitesimal method and regard the non-deformable sections as transformation matrices. Then the terminal position and attitude are calculated by multiplying the matrices in order. By loop assignment, we calculate the volume of the working spaces under various conditions. And we study the working space by quantitatively analyzing the impact factors, including load force and maximum input pressure. We design a DNN to solve the inverse kinematics and input the results of the forward kinematics for training, and the correlation coefficient reaches 0.945 in testing. Experiments validate the accuracy of the modeling and solution functions. Restricted by experimental conditions, we don't add high loads on the manipulator in the present work. In the future, we plan to carry out further experiments in the actual working environment.

Acknowledgments. This work is supported by the International Exchange Program of Harbin Engineering University for Innovation-oriented Talents Cultivation, the Natural Science Foundation of China under Grant 51875113, the Natural Science Joint Guidance Foundation of the Heilongjiang Province of China under Grant LH2019E027, "Jinshan Talent" Zhenjiang Manufacture 2025 Leading Talent Project. Thanks to Xiaozhi Gao et al. from HEU-DYNAVIO Joint Laboratory for their contribution to this paper.

References

[1] P. Polygerinos, N. Correll, S. A. Morin, B. Mosadegh, C. D. Onal, K. Petersen, M. Cianchetti, M. T. Tolley and R. F. Shepherd, "Soft robotics: Review of fluid-driven intrinsically soft devices; manufacturing, sensing, control, and applications in human-robot interaction," *Adv. Eng. Mater.* **19**(12), Article No. 1700016 (2017).

[2] S. Aracri, F. Giorgio-Serchi, G. Suaria, M. E. Sayed, M. P. Nemitz, S. Mahon and A. A. Stokes, "Soft robots for ocean exploration and offshore operations: A perspective," *Soft Rob.* ahead of print.

[3] Z. Peng and J. Huang, "Soft rehabilitation and nursing-care robots: A review and future outlook," *Appl. Sci.-Basel* **9**(15) (2019).

[4] Z. Jing, L. Qiao, H. Pan, Y. Yang and W. Chen, "An overview of the configuration and manipulation of soft robotics for on-orbit servicing," *Sci. China-Inf. Sci.* **60**(5), 1–19 (2017).

https://doi.org/10.1017/S0263574721000989 Published online by Cambridge University Press

[5] R. J. Webster, III and B. A. Jones, "Design and kinematic modeling of constant curvature continuum robots: A review," *Int. J. Rob. Res.* **29**(13), 1661–1683 (2010).
[6] C. Della Santina, R. K. Katzschmann, A. Bicchi, D. Rus and IEEE, "Dynamic control of soft robots interacting with the environment," 2018 IEEE International Conference on Soft Robotics (RoboSoft) (2018) pp. 46–53.
[7] H. Wang, B. Yang, Y. Liu, W. Chen, X. Liang and R. Pfeifer, "Visual servoing of soft robot manipulator in constrained environments with an adaptive controller," IEEE-ASME Trans. *Mech.* **22**(1), 41–50 (2017).
[8] C. Della Santina, A. Bicchi and D. Rus, "On an improved state parametrization for soft robots with piecewise constant curvature and its use in model based control," *IEEE Rob. Autom. Lett.* **5**(2), 1001–1008 (2020).
[9] F. Connolly, P. Polygerinos, C. J. Walsh and K. Bertoldi, "Mechanical programming of soft actuators by varying fiber angle," *Soft Rob.* **2**(1), 26–32 (2015).
[10] T. Hassan, M. Cianchetti, M. Moatamedi, B. Mazzolai, C. Laschi and P. Dario, "Finite-element modeling and design of a pneumatic braided muscle actuator with multifunctional capabilities," IEEE-ASME Trans. Mech. 24(1), 109–119 (2019).
[11] T. Nozaki and T. Noritsugu, "Motion analysis of McKibben type pneumatic rubber artificial muscle with finite element method," *Int. J. Autom. Technol.* **8**(2), 147–158 (2014).
[12] A. Shiva, S. M. H. Sadati, Y. Noh, J. Fras, A. Ataka, H. Wurdemann, H. Hauser, I. D. Walker, T. Nanayakkara and K. Althoefer, "Elasticity versus hyperelasticity considerations in quasistatic modeling of a soft finger-like robotic appendage for real-time position and force estimation," *Soft Rob.* **6**(2), 228–249 (2019).
[13] A. Stilli, E. Kolokotronis, J. Fras, A. Ataka, K. Althoefer and H. A. Wurdemann, "Static Kinematics for an Antagonistically Actuated Robot Based on a Beam-Mechanics-based Model," 2018 IEEE/RSJ International Conference on Intelligent Robots and Systems (IROS) (2018) pp. 6959–6964.
[14] P. S. Gonthina, A. D. Kapadia, I. S. Godage, I. A. Walker and IEEE, "Modeling Variable Curvature Parallel Continuum Robots Using Euler Curves," 2019 International Conference on Robotics and Automation (ICRA) (2019) pp. 1679–1685.
[15] M. Alebooyeh and R. J. Urbanic, "Neural network model for identifying workspace, forward and inverse kinematics of the 7-DOF YuMi 14000 ABB collaborative robot," *IFAC Papersonline* **52**(10), 176–181 (2019).
[16] M. Rolf and J. J. Steil, "Efficient exploratory learning of inverse kinematics on a bionic elephant trunk," *IEEE Trans. Neural Networks Learn. Syst.* **25**(6), 1147–1160 (2014).
[17] A. R. J. Almusawi, L. C. Dulger and S. Kapucu, "A new artificial neural network approach in solving inverse kinematics of robotic arm (Denso VP6242)," *Comput. Intell. Neurosci.* Article No. 5720163 (2016).
[18] W. He, Y. Ouyang and J. Hong, "Vibration control of a flexible robotic manipulator in the presence of input deadzone," *IEEE Trans. Ind. Inf.* **13**(1), 48–59 (2017).
[19] Z. Cao, Q. Xiao, R. Huang and M. Zhou, "Robust neuro-optimal control of underactuated snake robots with experience replay," *IEEE Trans. Neural Networks Learn. Syst.* **29**(1), 208–217 (2018).
[20] H. Wang, H. Xu, F. Yu, X. Li, C. Yang, S. Chen, J. Chen, Y. Zhang and X. Zhou, "Modeling and Experiments on the Swallowing and Disgorging Characteristics of an Underwater Continuum Manipulator," *2020 IEEE International Conference on Robotics and Automation (ICRA)* (2020) pp. 2946–2952.
[21] C. Ching-Ping and B. Hannaford, "Static and Dynamic Characteristics of McKibben Pneumatic Artificial Muscles," *Proceedings of the 1994 IEEE International Conference on Robotics and Automation*, vol. 281 (1994) pp. 281–286.
[22] E. G. Hocking and N. M. Wereley, "Analysis of nonlinear elastic behavior in miniature pneumatic artificial muscles," *Smart Mater. Struct.* **22**(1), Article No. 014016 (2012).
[23] C. S. Kothera, M. Jangid, J. Sirohi and N. M. Wereley, "Experimental characterization and static modeling of McKibben actuators," *J. Mech. Des.* **131**(9), Article No. 091010 (2009).
[24] B. K. S. Woods, C. S. Kothera and N. M. Wereley, "Wind tunnel testing of a helicopter rotor trailing edge flap actuated via pneumatic artificial muscles," *J. Intell. Mater. Syst. Struct.* **22**(13), 1513–1528 (2011).
[25] Z. Gong, J. Cheng, X. Chen, W. Sun, X. Fang, K. Hu, Z. Xie, T. Wang and L. Wen, "A bio-inspired soft robotic arm: Kinematic modeling and hydrodynamic experiments," *J. Bionic Eng.* **15**(2), 204–219 (2018).
[26] B. A. Jones and I. D. Walker, "Kinematics for multisection continuum robots," *IEEE Trans. Rob.* **22**(1), 43–55 (2006).
[27] S. Sheikhi, M. Shojaeifard and M. Baghani, "Finite bending and straightening of hyperelastic materials: Analytical solution and FEM," *Int. J. Appl. Mech.* **11**(9) (2019).

Cite this article: C. Yang, H. Xu, X. Li and F. Yu (2022). "Kinematic modeling and solution of rigid-flexible and variable-diameter underwater continuous manipulator with load", Robotica **40**, 1020–1035. https://doi.org/10.1017/S0263574721000989
https://doi.org/10.1017/S0263574721000989 Published online by Cambridge University Press